Akshay Kale[1]
Le Song[2]
Xinyu Lu[1]
Liandong Yu[2]*
Guoqing Hu[3,4]
Xiangchun Xuan[1]

[1]Department of Mechanical Engineering, Clemson University, Clemson, USA
[2]School of Instrument Science and Opto-electronic Engineering, Hefei University of Technology, Hefei, P. R. China
[3]LNM, Institute of Mechanics, Chinese Academy of Sciences, Beijing, P. R. China
[4]School of Engineering Science, University of Chinese Academy of Sciences, Beijing, P. R. China

Received August 28, 2017
Revised September 25, 2017
Accepted October 13, 2017

Research Article

Electrothermal enrichment of submicron particles in an insulator-based dielectrophoretic microdevice

Insulator-based dielectrophoresis (iDEP) exploits in-channel hurdles and posts etc. to create electric field gradients for various particle manipulations. However, the presence of such insulating structures also amplifies the Joule heating in the fluid around themselves, leading to both temperature gradients and electrothermal flow. These Joule heating effects have been previously demonstrated to weaken the dielectrophoretic focusing and trapping of microscale and nanoscale particles. We find that the electrothermal flow vortices are able to entrain submicron particles for a localized enrichment near the insulating tips of a ratchet microchannel. This increase in particle concentration is reasonably predicted by a full-scale numerical simulation of the mass transport along with the coupled charge, heat and fluid transport. Our model also predicts the electric current and flow pattern in the fluid with a good agreement with the experimental observations.

Keywords:
Electrokinetic / Electrothermal flow / Joule heating / Microfluidics / Particle enrichment
DOI 10.1002/elps.201700342

1 Introduction

In recent years, the scope of lab-on-a-chip applications has been significantly extended to the fields of medical diagnostics, biotechnology, and chemistry [1–3]. Specifically, these applications have been extensively targeted towards achieving selective manipulation of a wide variety of particles (a general term of, for example, biomarkers [4], cells [5], macromolecules [6] etc.) within physiological media that have substantial range of electric conductivities. Electrokinetic manipulation methodologies have been proven effective in serving this purpose [7–10] owing to the simple nature of their operation and integration as well as their conformity to lab-on-a-chip systems, allowing for a substantial reduction in the fluid volume handled [11–13]. Particularly among those, dielectrophoresis (DEP), which refers to the motion of a polarizable particle in electric field gradients [14–16], has emerged as a promising technology due to its label-free nature and high selectivity as a direct consequence of its dependence on the electric properties of particles [17–21].

The electric field gradients in DEP microdevices are commonly introduced by creating voltage drops across in-channel micro-electrodes (i.e., electrode-based DEP or eDEP) [22–24], or by using in-channel micro-insulators to locally amplify the electric field applied across the electrodes in channel-end fluid reservoirs (i.e., insulator-based DEP or iDEP) [25–27]. The iDEP devices prove advantageous over eDEP devices primarily due to their metal-free fabrication and lesser sensitivity to electrode fouling [28, 29]. The effectiveness of iDEP microdevices in focusing [30], trapping [31, 32], patterning [33], concentration [34–36], separation and sorting [37–40] particles (both synthetic and biological) is well-established. However, the difficulty of particle manipulation, particularly trapping and concentration, using DEP increases as the particle size gets small because the dielectrophoretic force scales with the particle volume [41,42]. Hence, a proportionally stronger electric field (as well as gradient) is essential to compensate for the weak dielectrophoretic force and facilitate the trapping of smaller (e.g., submicron and even nanoscale) particles [43]. Both eDEP [44] and iDEP [31, 32] microdevices have been demonstrated for this purpose, where, however, weakly conductive buffer solutions have to be used as the suspending medium in order to minimize Joule heating and the induced negative thermal effects [27].

Joule heating is an inevitable phenomenon of resistive heat generation in electric field-driven fluid flows [45, 46]. This volumetric internal heat source is proportional to the

Correspondence: Professor Xiangchun Xuan, Department of Mechanical Engineering, Clemson University, Clemson, SC 29634-0921, USA
Fax: +1-864-656-7299
E-mail: xcxuan@clemson.edu

Abbreviations: AC, alternating current; **DC**, direct current; **DEP**, dielectrophoresis; **iDEP**, insulator-based dielectrophoresis; **PDMS**, polydimethylsiloxane

*Additional corresponding author: Professor Liandong Yu
E-mail: liandongyu@hfut.edu.cn

Color Online: See the article online to view Figs. 1–7 in color.

square of the applied electric field. It becomes non-uniform around the insulators in iDEP microdevices and results in temperature gradients within the buffer [47, 48], which in turn induces gradients in temperature dependent fluid properties (e.g., conductivity, permittivity and viscosity etc. [49]). The interaction of these property gradients with electric field leads to a volumetric body force that perturbs the otherwise linear electrokinetic flow [50]. The resulting fluid flow is often called electrothermal flow [51], which manifests itself in the form of counter-rotating vortices at the insulating tips under strong Joule heating effects (due to either a high electric field or a high electric conductivity) [52, 53]. The velocity of electrothermal fluid flow is proportional to the fourth power of electric field, and hence grows at a much faster rate than that of particle DEP (scales as the second order of electric field) [50]. Joule heating has been recently demonstrated to weaken the dielectrophoretic focusing and trapping of microscale [49, 54–56] and nanoscale [57] particles in iDEP microdevices. It has also been shown to rearrange the dielectrophoretic trapping zone of microparticles [58]. Further, the resulting electrothermal fluid flow exerts its own drag force on the suspended particles apart from the dielectrophoretic force. Such a long-range fluid sampling has been demonstrated to assist the stirring and transport of biomolecules toward the sensing electrode [59].

This work demonstrates the feasibility of Joule heating-enabled electrothermal trapping and enrichment of submicron particles at the insulating tips of a ratchet microchannel. We also develop a full-scale numerical model to simulate the coupled fluid, charge and heat transport phenomena involved in the process. More importantly, we attempt to employ the convection-diffusion equation to simulate the mass transport of submicron particles within the fluid flow. The obtained concentration field can be used to understand the development of particle enrichment in the ratchet microchannel.

2 Materials and methods

2.1 Microchannel fabrication

Figure 1A shows a top-view picture of the ratchet microchannel used in our experiments. The channel was fabricated with polydimethylsiloxane (PDMS) using the standard soft lithography technique, where the mold was made with a negative SU-8 photoresist (MicroChem Corp.). It is overall 7 mm long and 500 μm wide with a circular extension of 5 mm diameter at each end. An array of twenty conjunct symmetric ratchets is patterned centrally on both walls of the microchannel along the length direction. Each ratchet is 250 μm long and extends 200 μm into the channel, leading to twenty equally spaced constrictions of width 100 μm (see the inset of Fig. 1A). The fabricated microchip has three layers as schematically illustrated in Fig. 1B: 2 mm thick PDMS slab on the top, 10 μm thick PDMS film in the middle and 1 mm thick glass slide on the bottom. The microchannel is sandwiched in between the PDMS slab and the PDMS film, rendering uniform and

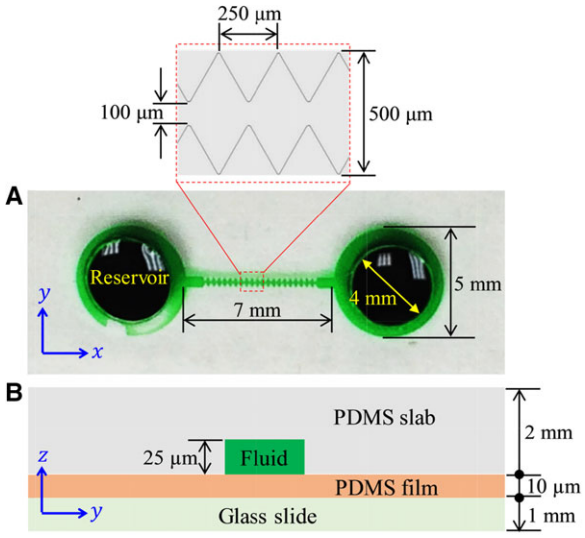

Figure 1. Top view picture (A, the ratchet microchannel and reservoirs are filled with green food dye for clarity) and cross-sectional view schematic (B, not to scale) of the microfluidic chip used in experiments. The inset shows the dimensions of the ratchets. Other important dimensions of the microchannel and substrates are also included.

identical surface properties of the four walls that surround the fluid. The 4 mm-diameter reservoir wells are through holes of the PDMS slab that were cut over the pre-defined circular extensions to the channel using a punch (see Fig. 1A).

2.2 Particle handling

A 2.5 mM phosphate buffer was used as the carrier fluid, whose electric conductivity and pH value were measured as 500 μS/cm and 7.4, respectively, at room temperature. Fluorescent polystyrene particles of 0.5 μm diameter (G500, Thermo Scientific) were added to the buffer to prepare the final solution. A high speed vortex mixer (Fischer Scientific) was used, before beginning each experiment, to ensure a uniform suspension of the particles in the fluid. The liquid levels in the two reservoirs were carefully balanced to eliminate the effects of pressure driven flow. DC-biased AC voltages were generated by using a power supply (Trek, 609E-6) and a function generator (Agilent Technologies, 3320 A). The resulting DC electric field drives the electroosmotic flow of the fluid and the electrophoretic motion of the tracing particles. In contrast, both the DC and AC electric fields contribute to Joule heating (and hence the electrothermal flow) and DEP. Platinum electrodes connected to this voltage supply system were kept in good contact with the solution in the reservoirs to produce the electric field. The DC voltage was fixed at 50 V while the AC voltage at 1 kHz was increased successively from 0 to 1200 V. The experiments were performed under a high intensity fluorescent lamp (Nikon Intensilight C-HGFI) to ensure visibility of the submicron particles under an inverted microscope (Nikon Eclipse TE2000U, Nikon Instruments). A CCD camera (Nikon DS-Qi1Mc) attached to the microscope

was used to generate video recordings at a rate of 15 fps with a 40 ms exposure time. Processing of the videos and subsequent generation of snapshot/superimposed images were both done using the Nikon image processing software (NIS-Elements AR 2.30).

2.3 Measurement of the channel wall and particle zeta potentials

The zeta potential of the microchannel walls was measured in a straight rectangular microchannel, which was fabricated with exactly the same procedure as described above, using the current-monitoring method [60]. Briefly, 2 mM phosphate buffer was prepared and introduced into one of the reservoirs, through which the channel was filled up by capillary action. The buffer of the present interest, i.e., 2.5 mM, with an equal volume to 2 mM buffer was immediately filled in the other reservoir till the two reservoir levels were balanced. It was then pumped at a low DC electric field (which eliminates the heating influence) to displace 2 mM buffer from the microchannel. The resulting increase in electric current was measured for about 1 min and the current-time graph generated was found to be linear. The slope of the graph was used to obtain the wall zeta potential, giving the value of −45 mV. The particle zeta potential was calculated by measuring the electrokinetic velocity of 0.5 μm diameter particles in the same test channel at low DC electric fields. The obtained value of electrokinetic mobility, which was determined from the slope of the linear curve of electrokinetic particle velocity-electric field, was then used to evaluate the difference between the wall and particle zeta potentials, leading to −65 mV for the latter. As the magnitude of the particle zeta potential is greater than that of the wall zeta potential, particles moves against the direction of electroosmotic fluid flow due to their faster and opposite electrophoretic motion in our experiments.

2.4 Numerical

2.4.1 Governing equations

The inevitable phenomenon of Joule heating in electroosmotic fluid flows through iDEP microdevices, and the associated variations in the temperature dependent fluid properties, such as electric conductivity σ, electric permittivity ε, and dynamic viscosity η, are well established [49–53, 55–59]. The non-uniform cross section of the ratchet microchannel results in an inhomogeneous temperature field, which generates fluid property gradients in the vicinity of the constrictions. At high voltages, these gradients may be strong enough to induce electrothermal flow vortices in the fluid [49], and thus affect the motion of particles suspended therein [52, 53]. The fluid motion in iDEP devices is governed by the coupled system of the electric current conservation equation, energy equation, and incompressible Navier-Stokes equations [49–51], which are presented below. The mathematical details for these equations are referred to our previous works [55, 56].

$$\nabla \cdot \left(\sigma \mathbf{E} + \frac{\partial (\varepsilon \mathbf{E})}{\partial t} \right) = 0 \tag{1}$$

$$\rho C \left(\frac{\partial T}{\partial t} + \mathbf{u} \cdot \nabla T \right) = \nabla \cdot (k \nabla T) + \sigma \mathbf{E}^2 \tag{2}$$

$$\nabla \cdot \mathbf{u} = 0 \tag{3a}$$

$$\rho \left(\frac{\partial \mathbf{u}}{\partial t} + (\mathbf{u} \cdot \nabla) \mathbf{u} \right) = -\nabla p + \nabla \cdot (\eta \nabla \mathbf{u}) + \rho_E \mathbf{E} - \frac{1}{2} \mathbf{E}^2 \nabla \varepsilon \tag{3b}$$

Here, Eq. (1) is for the electric field, $\mathbf{E} = -\nabla \phi$, inside the fluid only with ϕ the being electric potential; Eq. (2) is for the temperature field of both the fluid and the (glass and PDMS) substrates, where ρ, C, T and k are the mass density, heat capacity, temperature and thermal conductivity, respectively; Eqs. (3a) and (3b) are for the fluid velocity field, $\mathbf{u}$, and pressure field, p, where $\rho_E = \nabla \cdot (\varepsilon \mathbf{E})$ is the free charge density.

Considering the small size of the submicron particles used in our experiments, we employ the convection-diffusion equation to account for the effects of both fluid convection and Brownian diffusion on particle transport,

$$\frac{\partial c}{\partial t} + \nabla \cdot (\mathbf{u}_p c) = \nabla \cdot (D \nabla c) \tag{4}$$

$$\mathbf{u}_p = \mathbf{u} + \mathbf{u}_{EP} + \mathbf{u}_{DEP} \tag{5a}$$

$$\mathbf{u}_{EP} = \frac{\varepsilon \zeta_p}{\eta} \mathbf{E}_{DC} \tag{5b}$$

$$\mathbf{u}_{DEP} = \frac{\varepsilon d^2}{12\eta} \left(\frac{\sigma_p - \sigma}{\sigma_p + 2\sigma} \right) \nabla \mathbf{E}^2 \tag{5c}$$

where D is the diffusion coefficient of the particles; $\mathbf{u}_p$ in Eq. (5a) is the particle velocity due to fluid flow, $\mathbf{u}$, particle electrophoresis, $\mathbf{u}_{EP}$, in Eq. (5b) and particle DEP, $\mathbf{u}_{DEP}$ in Eq. (5c); ζ_P and σ_p are the zeta potential and electric conductivity of the particles, respectively; $\mathbf{E}_{DC}$ is the DC electric field. Note that we have assumed an equal value of $\mathbf{u}_{DEP}$ for DC and low-frequency AC electric fields [50]. The use of Eq. (4) enables the simulation of the increased particle concentration during the trapping process, which is unavailable with the often-used Lagrangian Tracking Method that can only track the trajectory of single particles [55, 56, 61]. The effects of AC voltage are incorporated into the model by defining a ratio of the applied RMS AC voltage, ϕ_{AC}, to the applied DC voltage, ϕ_{DC} in Eq. (6),

$$r = \frac{\phi_{AC}}{\phi_{DC}} \tag{6}$$

The modifications of the governing equations after having incorporated the AC voltage effect have been elaborated in detail in our previous works [55, 56] and are hence not repeated here.

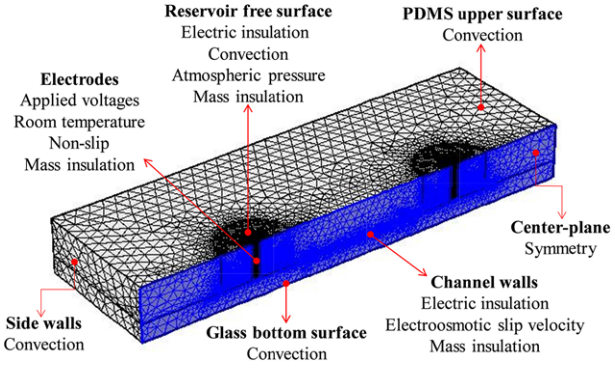

Figure 2. Computational geometry (note the plane of symmetry is highlighted in blue) for the numerical model and the boundary conditions for the governing equations, i.e., Eqs. (1)-(4).

2.4.2 Computational domain and boundary conditions

Due to the symmetry of our microchip about the center-plane of the ratchet microchannel, we considered only half of the experimental device in the simulation. The meshed 3D computational geometry along with the applied boundary conditions is shown in Fig. 2. The full length and width of the geometry are 3 and 0.8 cm, respectively, while the depth of each layer in the geometry is highlighted in Fig. 1B. Owing to the high electric conductivity, a platinum electrode does not develop an electric field within itself. Hence, the two electrodes are each modeled as a hole and provided with a Dirichlet boundary condition of the applied voltage. The microchannel and reservoir walls are assumed to be electrically insulated. The fluid flow is modeled with the well-established Smoluchowski electroosmotic slip velocity condition on the entire wetted PDMS walls [12, 13], given by Eq. (7),

$$\mathbf{u}_{EO} = -\frac{\varepsilon\zeta_w}{\eta}\mathbf{E}_{DC} \tag{7}$$

with ζ_w being the wall zeta potential. The free surfaces of the reservoirs are set to be at atmospheric pressure, thereby eliminating the pressure gradient. For the energy equation, the entire outer surface of the microchip (including the free surfaces of the reservoirs) is provided with a natural convection boundary condition. As to the concentration equation, the microchannel and reservoir walls are assumed insulating for mass transport. An initially uniform particle concentration of 1 mol/m^3 (by default, actually regardless of the unit in our model) is assumed within the whole fluid, so that the concentration field simply rearranges itself within the fluid domain with time.

2.4.3 Material properties

The temperature dependences of the important fluid properties are defined in Eqs. (8)–(10) [45, 46, 52, 55, 56],

$$\varepsilon = \varepsilon_0\left[1 + \alpha\left(T - T_0\right)\right] \tag{8}$$

$$\sigma = \sigma_0\left[1 + \beta\left(T - T_0\right)\right] \tag{9}$$

$$\eta = 2.761 \times 10^{-6}\exp\left(\frac{1713}{T}\right) \tag{10}$$

where ε_0 and σ_0 represent the fluid permittivity and electric conductivity at the room temperature, T_0, with α and β being their respective temperature coefficients. The electric conductivity, σ_p in Eq. (5c), for polystyrene particles of diameter, d, is defined in Eq. (11) [63],

$$\sigma_p = \sigma_{pbulk} + 4\frac{k_S}{d} \tag{11}$$

where the bulk conductivity, σ_{pbulk}, is negligible for polystyrene, and the surface conductance, k_S, is taken as 1 nS [64]. As the calculated value of σ_p (80 μS/cm) is smaller than the measured electric conductivity of the fluid (500 μS/cm), particles exhibit negative DEP in our experiments. In addition, the diffusion coefficient of particles is modeled using the Stokes-Einstein relation in Eq. (12),

$$D = \frac{k_B T}{3\pi\eta d} \tag{12}$$

where k_B is Boltzmann's constant. The values of the material properties involved in the numerical simulation are provided in Table 1.

2.4.4 Numerical method

The 3D numerical model was developed in COMSOL® Multiphysics 4.4. The temperature, electric and flow fields were simulated for a steady state, while the concentration field was simulated in a transient model by using the particle velocity computed from the steady-state field variable distributions. Although it would be more rigorous to use a fully transient model, this simplification is expected to provide a reasonable match to the experimental observations with a much less computational cost. This is justified using a scaling analysis of the time required for each of the fields to develop. Following the analysis procedure in Ge et al. [62], the development time scales for the field variables are computed and listed in Table 2, where D_h is the hydraulic diameter of the microchannel as traditionally defined. Clearly, the fluid velocity and temperature fields develop in the fluid domain within 100 ms, which is significantly quicker than the observation time scale. In contrast, the concentration field requires a development time that is several orders of magnitude greater than that of the velocity and temperature fields, thereby justifying the use of a semi-transient model as noted above. The presence of multiple constrictions in the ratchet microchannel produces strong localized gradients of temperature, electric and velocity fields, necessitating the use of a very fine mesh in the fluid domain. The model was tested with successive mesh refinements to ensure a grid-independent convergence using over 6 million elements. Clemson's supercomputing facility i.e. the PALMETTO cluster, was utilized to solve the model. Simulation cases were run with a RAM memory of 500 GB

Table 1. Material properties used in numerical simulation

Material	Symbol	Description	Value	Unit
PDMS	k	Thermal conductivity of PDMS	0.15	W/mK
	ρ	Mass density of PDMS	1030	kg/m^3
	C	Specific heat of PDMS	1460	J/kgK
	ζ_W	Wall zeta potential	−45	mV
Glass	k	Thermal conductivity of glass	1.38	W/mK
	ρ	Mass density of glass	2203	kg/m^3
	C	Specific heat of glass	703	J/kgK
Fluid	k	Thermal conductivity of fluid	0.6	W/mK
	ρ	Mass density of fluid	1000	kg/m^3
	C	Specific heat of fluid	4187	J/kgK
	ε_0	Fluid permittivity at room temperature	7.1E-10	F/m
	α	Temperature coefficient of permittivity	−0.0046	1/K
	σ_0	Fluid electric conductivity at room temperature	500	μS/cm
	β	Temperature coefficient of electric conductivity	0.02	1/K
	T_0	Room temperature	293	K
Particle	d	Particle size	0.5	μm
	σ_p	Particle electric conductivity	80	μS/cm
	ζ_P	Particle zeta potential	−65	mV

Table 2. Development time scales for the field variables within the fluid in the microchannel

Field variable	Development time scale	Order of magnitude (sec)
Velocity	$\frac{D_H^2}{(\eta/\rho)}$	$O(10^{-3})$
Temperature	$\frac{D_H^2}{(k/\rho C)}$	$O(10^{-2})$
Concentration	$\frac{D_H^2}{D}$	$O(10^3)$

shared over 24 parallel operating cores to return a solution after 52 clock hours.

3 Results and discussion

3.1 Particle enrichment

Figure 3A shows a comparison of the experimentally obtained snapshots and the numerically predicted concentration contours of 0.5 μm diameter particles in the ratchet microchannel at the observation times of 2.5 and 10 s, respectively. The applied voltage is 50 V DC-biased 1200 V AC, yielding an average electric field of around 179 V/mm along the microchannel. The channel outlet (which is actually the inlet for the particles) is chosen for representation because the ratchets therein are the first ones to interact with the incoming flow of particles. The increasing amount of particle entrainment within the flow circulations near the tips of those ratchets is evident from the experimental snapshots at different times. Interestingly the particles are seen to be trapped almost exclusively in the upstream vortices at each ratchet pair. This behavior can be directly attributed to the direction of rotation of the electrothermal vortices, as highlighted on the images in Fig. 3A (left column, see also the cartoon in Fig. 3B). The downstream electrothermal drag forces at the periphery of the vortices tend to pull the incoming particle stream with the flow and then push it to the upstream region. However, the electrothermal flow in the upstream region rotates in an opposite sense and performs the function of momentarily retarding the particle motion, thereby facilitating a subsequent entrainment.

The numerical simulations in Fig. 3A (right column) are seen to predict the experimental trend of increasing number of trapped submicron particles with time. We measured the intensity of particle fluorescence from the experimental images, and found a 3.5-time increase in the normalized fluorescence intensity (background-corrected). This enrichment value is comparable to the numerically predicted nearly 4-fold increase in the particle concentration at each vortex after 10 s (see the color map in Fig. 3A). A slight difference to be noted, however, is that the numerical simulation also predicts an increase in the particle concentration within the downstream vortices, though much weaker than the upstream ones. This discrepancy from experimental observations may be attributed to the fact that while the particles are a discrete entity suspended in a fluid continuum, the concentration equation assumes a continuous distribution of both the particles and the fluid. Hence, the conservation of convection dominated mass transport, as in this case, requires a local concentration increase at low particle velocity points that may still exist at the cores of the downstream vortices.

It is important to note that 0.5 μm diameter particles experience negative DEP in the current experiment because the suspending fluid is electrically more conductive. The consequence of DEP alone is thus to push the particles away from the ratchet tips, where the local electric field is the

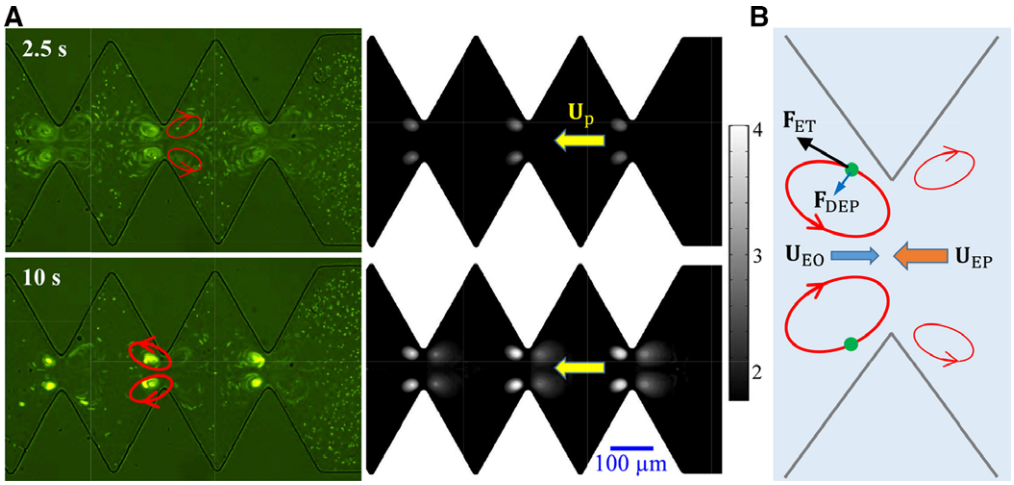

Figure 3. (A) Comparison of experimentally obtained snapshot images (left column) and numerically predicted concentration fields (right column) of 0.5 μm particles at the fluid outlet of the ratchet microchannel. The applied voltage is 50 V DC-biased 1200 V AC. (B) Cartoon highlighting the forces experienced by a particle at the tip of the ratchet microchannel, where F_{ET} and F_{DEP} are the electrothermal drag force and dielectrophoretic force, respectively. The overall direction of electroosmotic fluid flow (u_{EO}) in the microchannel is from left to right, opposite to that of particle motion (u_p, which is from right to left) due to the stronger right-to-left electrophoretic motion (u_{EP}) as highlighted by the block arrows. The arrowed loops highlight the circulating directions of the downstream (thinner lines, weak particle entrainment) and upstream (thicker lines, strong particle enrichment) electrothermal flow vortices.

maximum [33], and focus them into a tighter stream near the center-plane of the microchannel [30]. In other words, it is the Joule heating induced electrothermal flow circulations that lead to the trapping and enrichment of submicron particles in the ratchet microchannel. This, as schematically illustrated in Fig. 3B, is different from the observations in our previous works [54–56], where Joule heating effects have been demonstrated to reduce the electrokinetic focusing and trapping of micron-sized particles in ratchet-like constriction microchannels. Since the motion of particles in the ratchet region is influenced chiefly by the electrothermal drag force, $\mathbf{F}_{ET}$, and the dielectrophoretic force, $\mathbf{F}_{DEP}$, we define a dimensionless number, γ, as the ratio of these two forces acting on the particles,

$$\gamma = \left| \frac{\mathbf{F}_{ET}}{\mathbf{F}_{DEP}} \right| \tag{13}$$

This ratio is expected to provide an insight on the dominance of one manipulative force over the other. We can do a simple scaling analysis [50, 51],

$$\mathbf{F}_{ET} \sim \mathbf{E}^2 d\nabla T \tag{14}$$

$$\mathbf{F}_{DEP} \sim \mathbf{E}^2 d^3 \tag{15}$$

Thus, the dimensionless force ratio in Eq. (13) can be rewritten using Eqs. (14) and (15) as

$$\gamma \propto \frac{\lfloor \nabla T \rfloor}{d^2} \tag{16}$$

Clearly, the electrothermal drag force can become dominant over the dielectrophoretic force for small particle sizes, which explains why submicron particles can be captured inside the electrothermal flow circulations in Fig. 3A. However, for large particles, DEP is still dominant though being reduced by Joule heating effects, which has been experimentally and numerically demonstrated in our previous works [54–56]. It is interesting to see whether, as indicated by the increasing value of γ in Eq. (16) for a reduced particle size, nanoparticles can be electrothermally trapped and enriched. We will test this hypothesis in our future work.

Figure 4 shows the experimentally obtained trapping patterns and numerically predicted concentration increases of 0.5 μm particles over the length of the ratchet microchannel. The data are obtained at 10 s after a 50 V DC-biased 1200 V AC voltage is imposed. Similar to the experimental observations in Fig. 3A, the particle trapping zones near the ratchet tips is seen to extend throughout the channel. Moreover, the particle enrichment takes place primarily inside the upstream vortices and seems to be insensitive to the ratchet position. In contrast, the simulation predicts that the particle enrichment also occurs in the downstream vortices near the channel outlet (i.e., the inlet of the particles), though very weak, while gradually fading away towards the channel inlet. This discrepancy from the experimental observation is again due to perhaps the assumption of a continuous particle phase in our model as noted above. Further studies are required toward resolving this issue.

3.2 Joule heating-induced temperature variations

To better understand the effects of Joule heating and the induced electrothermal flow on submicron particle enrichment, we also use the numerical model to study the other property fields in the ratchet microchannel. In a straight microchannel, the electric field generated due to a voltage drop is uniform. However, each pair of the ratchets fabricated in the microchannel acts as an insulating constriction and locally

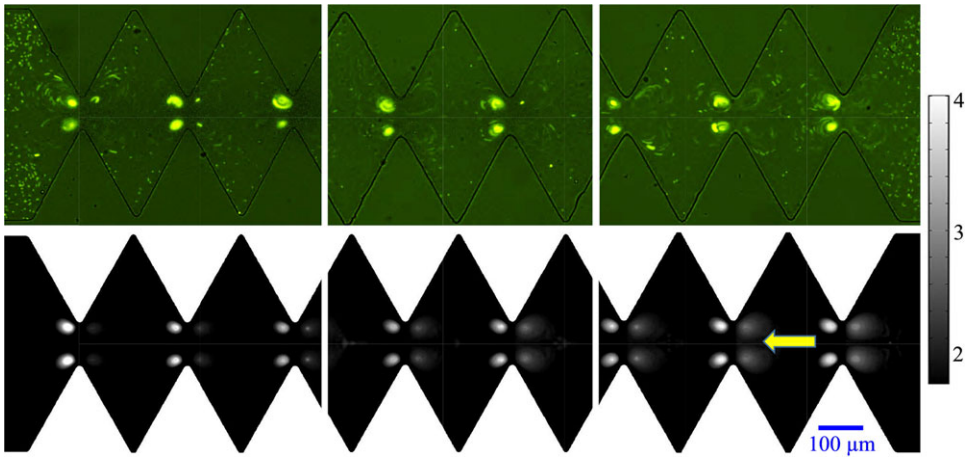

Figure 4. Experimental (top) and numerical (bottom) demonstration of electrothermal enrichment zones for 0.5 μm diameter particles at the fluid inlet (left column, particle outlet), middle (middle column), and fluid outlet (right column, particle inlet) of the ratchet microchannel under 50 V DC-biased 1200 V AC. The block arrow indicates the overall particle moving direction through the channel, which is opposite to the direction of fluid flow.

amplifies the electric field in accordance with the current conservation. This skewing leads to a periodic oscillation of electric field in the ratchet region, thereby providing multiple potential zones for manipulating the motion of particles. The regions of high electric field experience a stronger Joule heating ($\sim \mathbf{E}^2$), which elevates the local fluid temperature and should create multiple hotspots. However, each hotspot dissipates heat around itself in the channel, causing heat interactions between the adjacent hotspots. Moreover, the local generation of Joule heating over the length of the channel also contributes to the temperature increase. The net effect of both phenomena results into an apparently higher fluid temperature in the ratchet region along with a hotspot in between every pair of ratchet tips (see the inset plot of Fig. 5). The heat generated inside the fluid then dissipates into the surrounding through the substrates, leading to a temperature decay in the microchip with the increasing distance away from the microchannel (see Fig. 5).

At a fixed DC voltage, a higher AC-DC ratio results in a stronger temperature field over the microchip and further increases the electric current flowing through the buffer. Figure 6 compares the experimentally measured electric currents with the numerically predicted values under varying AC-DC ratios. The numerical results agree well with the experimentally measured values, both of which are, as expected, higher than the electric current in the absence of Joule heating effects. At low electric fields with weak Joule heating, the change in the temperature dependent electric conductivity is insignificant. As such, the electric current varies linearly with the AC-DC ratio. As Joule heating gets stronger at higher AC-DC ratios, the temperature field becomes significantly high to increase the electric conductivity of the buffer. The increased conductivity provides its own contribution to the electric current along with the AC-DC ratio itself, causing the current to increase non-linearly with electric field. Especially when the AC-DC ratio reaches 18 (i.e., 900 V AC as illustrated in Fig. 5), the numerical model begins to underestimate the electric current. One possible reason for this deviation is the irreversible change in the thermal properties of PDMS as it gets damaged due to Joule heating at increasing applied

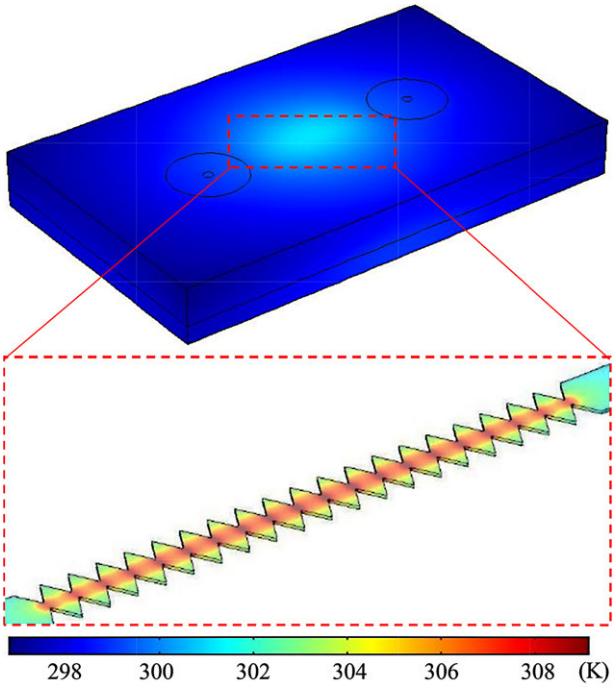

Figure 5. Numerically predicted steady-state temperature field in the microchip and inside the ratchet microchannel (inset) at 50 V DC / 900 V AC. Note that the full-chip image was obtained by mirroring the results about the plane of symmetry (see Fig. 2).

voltages. This degradation of PDMS with temperature is likely to make it more thermally resistive which would result in a higher fluid temperature than what is predicted by the model.

3.3 Electrothermal flow

Figure 7 demonstrates the experimentally observed and numerically predicted electrothermal flow in the form of particle streaklines at the middle of the ratchet microchannel. The DC voltage is fixed at 50 V while the AC voltage is varied from 600 to 1200 V. The flow field visualization experiments are

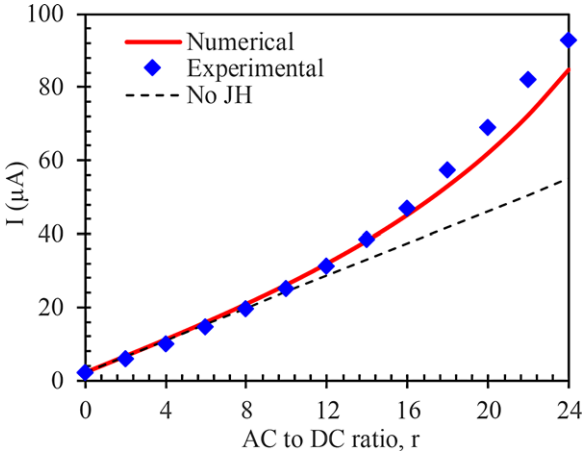

Figure 6. Comparison of the experimentally measured (symbols) and numerically predicted (solid line) electric current in the microchannel as a function of the applied AC to DC voltage ratio. The DC voltage is fixed at 50 V. The dashed line represents the electric current in the absence of Joule heating effects, which was obtained by linearly fitting the electric current values measured at the two smallest electric fields.

each run for 3 s only, such that the electrothermal enrichment of the tracing particles, if any, is still insignificant (see Fig. 3A). The fact that the electrothermal flow develops almost completely in the order of a few milliseconds (see Table 2) justifies the sufficiency of this small runtime. The instantaneous positions of the particles at every time instant over the length of the video are superimposed to generate the streak images in Fig. 7. It can be seen that up to 600 V AC, the electrothermal flow is not strong enough to overcome the local electrokinetic motion of particles. Joule heating effects start becoming significant as the AC voltage increases to 700 V, where the submicron tracing particles exhibit a slight bending at the fluid upstream of the ratchet tips. This deviation from the traditional linear electrokinetic flow is reasonably captured by the numerical simulation. The strength of the electrothermal flow increases at higher AC electric fields, and the vortices grow in size and speed as the AC voltages goes from 900 to 1200 V. The tracing of the vortices by the small particles illustrates the increasing dominance of the electrothermal drag force over the dielectrophoretic force at high AC voltages, which is consistent with the prediction of Eq. (16). A visual increase in the local fluorescence intensity of the particles at the location of the vortices is also apparent from the experimental images in Fig. 7 when the AC voltage is increased. This suggests an entrainment of the tracing submicron particles as time progresses, which is consistent with the analysis in Section 3.1.

4 Concluding remarks

We have presented a combined experimental and numerical investigation of the feasibility of electrothermal flows to manipulate the motion of submicron particles in a ratchet microchannel. A dimensionless force ratio is defined, which indicates that the electrothermal drag force becomes dominant over the dielectrophoretic force for small particle sizes under strong Joule heating. The resulting electrothermal flow vortices are demonstrated to entrain submicron particles within them for a localized enrichment at the fluid upstream of every pair of insulating ratchets. Moreover, the numerical simulation of the mass transport predicts this increase in particle concentration near the ratchet tips. However, our model assumes a continuous distribution of particles in the fluid, which leads to an additional pair of weakly increased concentration zone at the downstream electrothermal vortices of the ratchets. In addition, the numerical simulation of the coupled charge, heat and fluid transport predicts the electric current and flow pattern with a good agreement with the experimental observations. We are currently extending the demonstrated electrothermal trapping technique to nanoparticles. We are also studying how the particle enrichment can be further enhanced by, for example, changing the

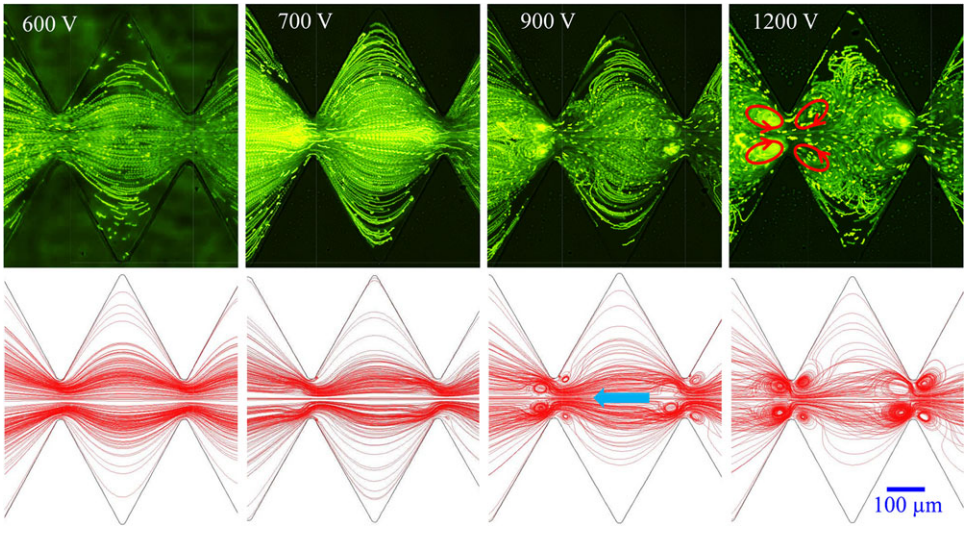

Figure 7. Experimentally obtained (top row) and numerically predicted (bottom row) streaklines of 0.5 μm particles demonstrating the development of electrothermal flow in the middle of the ratchet microchannel under varying 50 V DC-biased AC voltages (see the labeled RMS values on the experimental images). The arrowed loops on the upper right experiment image highlight the directions of electrothermal flow vortices. The block arrow on the bottom row indicates the overall particle moving direction through the channel (opposite to the direction of fluid flow).

symmetric ratchets to asymmetric ones [33]. Moreover, we will extend our recently developed 2D depth-averaged model [53, 65] to predict Joule heating enabled electrothermal enrichment of particles. Our demonstrated particle enrichment technique may open up new opportunities for the electrical and thermal control of macromolecules in iDEP microdevices for broader lab-on-a-chip applications.

This work is partially supported by NSF under Grant CBET-1704379 (X.X.), University 111 Project of China under Grant B12019 (L.Y.), and NSFC under grants 11272321 and 11572334 (G.H.). The support from the Open Fund of LNM (X.X. and G.H.) is also gratefully acknowledged.

The authors have declared no conflict of interest.

5 References

[1] Stone, H. A., Stroock, A. D., Ajdari, A., *Annu. Rev. Fluid Mech.* 2004, *36*, 381–411.

[2] Squires, T. M., Quake, S. R., *Rev. Modern Phys.* 2005, *77*, 977–1026.

[3] Yager, P., Edwards, T., Fu, E., Helton, K., Nelson, K., Tam, M. R., Weigl, B. H., *Nature* 2006, *442*, 412–418.

[4] Sheehan, P. E., Whitman, L. J., *Nano Lett.* 2005, *5*, 803–807.

[5] Salieb-Beugelaar, G. B., Simone, G., Arora, A., Philippi, A., Manz, A., *Anal. Chem.* 2010, *82*, 4848–4864.

[6] Holzel, R., *IET Nanobiotechnol.* 2009, *3*, 28–45.

[7] Bruin, G. J. M., *Electrophoresis* 2000, *21*, 3931–3951.

[8] Wong, P. K., Wang, T., Deval, J. H., Ho, C. M., *IEEE/ASME Trans. Mechatronics* 2004, *9*, 366–376.

[9] Masliyah, J. H., Bhattacharjee, S., *Electrokinetic and Colloid Transport Phenomena*, John Wiley & Sons, Inc., Hoboken, New Jersey 2006.

[10] Kang, Y., Li, D., *Microfluid. Nanofluid.* 2009, *6*, 431–460.

[11] Morgan, H., Green, N. G., *AC Electrokinetics: Colloids and Nanoparticles*, Research Studies, Williston, VT 2003.

[12] Li, D. *Electrokinetics in microfluidics*, Elsevier Academic Press, Burlington, MA (2004).

[13] Chang, H. C., Yeo, L. Y., *Electrokinetically Driven Microfluidics and Nanofluidics*, Cambridge University Press, New York (2010).

[14] Pohl, H. A., *Dielectrophoresis*, Cambridge University Press, Cambridge (1978).

[15] Gascoyne, P. R. C., Vykoukal, J., *Electrophoresis* 2002, *23*, 1973–1983.

[16] Pethig, R., *Biomicrofluid.* 2010, *4*, 022811.

[17] Hughes, M. P., *Electrophoresis* 2002, *23*, 2569–2582.

[18] Gagnon, Z. R., *Electrophoresis* 2011, *32*, 2466–2487.

[19] Pethig, R., *Adv. Drug Deliv. Rev.* 2013, *65*, 1589–1599.

[20] Dash, S., Mohanty, S., *Electrophoresis* 2014, *35*, 2656–2672.

[21] Adekanmbi, E. O., Srivastava, S. K., *Lab Chip* 2016, *16*, 2148.

[22] Gascoyne, P. R. C., Vykoukal, J., *Proc. IEEE Inst. Electr. Electron. Eng.* 2004, *92*, 22–42.

[23] Cetin, B., Li, D., *Electrophoresis* 2011, *32*, 2410–2427.

[24] Hughes, M. P., *Biomicrofluid.* 2016, *10*, 032801.

[25] Srivastava, S. K., Gencoglu, A., Minerick, A. R., *Anal. Bioanal. Chem.* 2010, *399*, 301–321.

[26] Regtmeier, J., Eichhorn, R., Viefhues, M., Bogunovic, L., Anselmetti, D., *Electrophoresis* 2011, *32*, 2253–2273.

[27] Romero-Creel, M. F., Goodrich, E., Polniak, D. V., Lapizco-Encinas, B. H., *Micromachines* 2017, *8*, 239.

[28] Chou, C. F., Zenhausern, F., *IEEE Eng. Med. Biology Mag.* 2003, *22*, 62–67.

[29] Li, M., Li, W. H., Zhang, J., Alici, G., Wen, W., J. Phys. D: Appl. Phys. 2014, *47*, 063001.

[30] Zhu, J., Xuan, X., *Electrophoresis* 2009, *30*, 2668–2675.

[31] Chou, C. F., Tegenfeldt, J. O., Bakajin, O., Chan, S. S., Cox, E. C., Darnton, N., Duke, T., Austin, R. H,, *Biophys. J.*, 2002, *83*, 2170–2179.

[32] Nakano, A., Camacho-Alanis, F., Ros, A., *Analyst* 2015, *140*, 860–868.

[33] Kale, A., Lu, X., Patel, S., Xuan, X., *J. Micromech. Microeng.* 2014, *24*, 075007.

[34] Barrett, L. M., Skulan, A. J., Singh, A. K., Cummings, E. B., Fiechtner, G. J., *Anal. Chem.* 2005, *77*, 6798–6804.

[35] Lapizco-Encinas, B. H., Davalos, R. V., Simmons, B. A., Cummings, E. B., Fintschenko, Y., *J. Microbiol. Methods* 2005, *62*, 317–326.

[36] Pysher, M. D., Hayes, M. A., *Anal. Chem.* 2007, *79*, 4552–4557.

[37] Lapizco-Encinas, B. H., Simmons, B. A., Cummings, E. B., Fintschenko, Y., *Anal. Chem.* 2004, *76*, 1571–1579.

[38] Lapizco-Encinas, B. H., Simmons, B. A., Cummings, E. B., Fintschenko, Y., *Electrophoresis* 2004, *25*, 1695–1704.

[39] Hawkins, B. G., Smith, A. E., Syed, Y. A., Kirby, B. J., *Anal. Chem.* 2007, *79*, 7291–7300.

[40] Kang, Y. J., Li, D. Q., Kalams, S. A., Eid, J. E., *Biomed. Microdev.* 2008, *10*, 243–249.

[41] Jesu´s-Pe´rez, N. M., Lapizco-Encinas, B. H., *Electrophoresis* 2011, *32*, 2331–2357.

[42] Jubery, T. Z., Srivastava, S. K., Dutta, P., *Electrophoresis* 2014, *35*, 691–713.

[43] Lapizco-Encinas, B. H., Rito-Palomares, M., *Electrophoresis* 2007, *28*, 4521–4538.

[44] Washizu, M., Suzuki, S., Kurosawa, O., *IEEE Trans. Industry App.* 1994, *30*, 835–843.

[45] Cetin, B., Li, D., *Electrophoresis* 2008, *29*, 994–1005.

[46] Xuan, X., *Electrophoresis* 2008, *29*, 33–43.

[47] Nakano, A., Luo, J., Ros, A., *Anal. Chem.* 2014, *86*, 6516–6524.

[48] Samy, R, Glawdel, T., Ren, C. L., *Anal. Chem.* 2008, *80*, 369–375.

[49] Hawkins, B. J., Kirby, B. J., *Electrophoresis* 2010, *31*, 3622–3633.

[50] Casterllanos, A., Ramos, A., Gonzalez, A., Green, N. G., Morgan, H., *J. Phys. D* 2003, *36*, 2584–2597.

[51] Green, N. G., Ramos, A., Morgan, H., *J. Phys. D* 2000, *33*, 632–641.

[52] Sridharan, S., Zhu, J., Hu, G., Xuan, X., *Electrophoresis* 2011, *32*, 2274–2281.

[53] Prabhakaran, R. A., Zhou, Y., Patel, S., Kale, A., Song, Y., Hu, G., Xuan, X., *Electrophoresis* 2017, *38*, 572–579.

[54] Zhu, J., Sridharan, S., Hu, G., Xuan, X., *J. Micromech. Microeng.* 2012, *22*, 075011.

[55] Kale, A., Patel, S., Hu, G., Xuan, X., *Electrophoresis* 2013, *34*, 674–683.

[56] Kale, A., Patel, S., Qian, S., Hu, G., Xuan, X., *Electrophoresis* 2014, *35*, 721–727.

[57] Chaurey, V., Rohani, A., Su, Y. H., Liao, K. T., Chou, C. F., Swami, N. S., *Electrophoresis* 2013, *34*, 1097–1104.

[58] Gallo-Villanueva, R., Sano, M., Lapizco-Encinas, B., Davalos, R., *Electrophoresis* 2014, *35*, 352–361.

[59] Chaurey, V., Polanco, C., Chou, C. F., Swami, N. S., *Biomicrofluid.* 2012, *6*, 012806.

[60] Almutairi, Z., Glawdel, T., Ren, C., Johnson, D., *Microfluid. Nanofluid.* 2009, *6*, 241–251.

[61] Qian, S., Ai, Y., *Electrokinetic Particle Transport in Micro-/Nanofluidics: Direct Numerical Simulation Analysis*, CRC Press 2012.

[62] Ge, Z., Yang, C., Tang, G., *Int. J. Heat Mass Transf.* 2010, *53*, 2722–2731.

[63] Hughes, M. P., Morgan, H., Flynn, M. F., J. Colloid Interf. *Sci.* 1999, *220*, 454–457.

[64] Ermolina, I., Morgan, H., J. Colloid Interf. *Sci.* 2005, *285*, 419–428.

[65] Song, L., Yu. L., Zhou, Y., Antao, A. R., Prabhakaran, R. A., Xuan, X., *Sci. Rep.* 2017, *7*, 46510.

